

Utilizing multiple scale models to improve predictions of extra-axial hemorrhage in the immature piglet

Gregory G. Scott¹ · Susan S. Margulies² · Brittany Coats¹

Received: 2 June 2015 / Accepted: 6 November 2015 / Published online: 19 November 2015
© Springer-Verlag Berlin Heidelberg 2015

Abstract Traumatic brain injury (TBI) is a leading cause of death and disability in the USA. To help understand and better predict TBI, researchers have developed complex finite element (FE) models of the head which incorporate many biological structures such as scalp, skull, meninges, brain (with gray/white matter differentiation), and vasculature. However, most models drastically simplify the membranes and substructures between the pia and arachnoid membranes. We hypothesize that substructures in the pia–arachnoid complex (PAC) contribute substantially to brain deformation following head rotation, and that when included in FE models accuracy of extra-axial hemorrhage prediction improves. To test these hypotheses, microscale FE models of the PAC were developed to span the variability of PAC substructure anatomy and regional density. The constitutive response of these models were then integrated into an existing macroscale FE model of the immature piglet brain to identify changes in cortical stress distribution and predictions of extra-axial hemorrhage (EAH). Incorporating regional variability of PAC substructures substantially altered the distribution of principal stress on the cortical surface of the brain compared to a uniform representation of the PAC. Simulations of 24 non-impact rapid head rotations in an immature piglet animal model resulted in improved accuracy of EAH prediction (to 94 % sensitivity, 100 % specificity), as well as a high accuracy in regional hemorrhage prediction (to 82–100 % sensitivity, 100 % specificity). We conclude that including a bifidelic PAC substructure variability in FE models of the

head is essential for improved predictions of hemorrhage at the brain/skull interface.

Keywords Subarachnoid space · Microstructure · Traumatic brain injury · Finite element modeling · Arachnoid trabeculae

1 Introduction

Traumatic brain injury (TBI) is a leading cause of death and disability in the USA (Faul et al. 2010). Etiologies include military conflict, motor vehicle crashes, assault, and sports-related trauma. A powerful tool commonly used in the investigation of TBI is finite element (FE) modeling. Researchers have developed comprehensive whole-head models of head injury which take into account many of the biological complexities of the head including scalp, skull, meninges, brain (with gray/white matter differentiation), and vasculature (Giordano et al. 2014; Ji et al. 2014; McAllister et al. 2011; Roth et al. 2008; Takhounts et al. 2008; Zhang et al. 2002, 2001). However, these studies fall short in how they represent the pia–arachnoid complex (PAC) and its interaction between the brain and the skull. Most commonly, the PAC is modeled as either a solid element or a fluid element. These idealized representations of the PAC may result in adequate estimations of brain stress or strain in the deeper structures of the brain, but likely cause finite element models to fall short in terms of injury prediction at the brain–skull interface. Coats et al. (2012) compared multiple idealized representations of the PAC, including elastic spring connectors and solid isotropic elements tied to the brain and skull, and evaluated their influence on predictions of brain/skull displacement and brain strain. While both elastic connectors and solid elements resulted in reasonable approximations of

✉ Brittany Coats
brittany.coats@utah.edu

¹ Department of Mechanical Engineering, University of Utah, 1495 E. 100 S., 1550 MEK, Salt Lake City, UT 84112, USA

² Department of Bioengineering, University of Pennsylvania, Philadelphia, PA, USA

brain/skull displacement, the elastic connectors were better at predicting intracranial hemorrhage based on the tensile strain of the connector. The sensitivity and specificity of intracranial hemorrhage predictions were 80 and 85 %, respectively. Localized, or regional, predictions of hemorrhage did not perform as well, and resulted in sensitivity and specificity values as low as 63 and 76 % in some regions. Despite this shortcoming, the [Cloots et al. \(2008\)](#), [Couper and Albermani \(2008\)](#), [Kuijpers et al. \(1995\)](#), [Paolini et al. \(2009\)](#), [Wittek and Omori \(2003\)](#) study, and other studies investigating the influence of the brain–skull interface on prediction of brain injury agree that attention to the biofidelic representation of this interface is critical to the accurate prediction of TBI. Progress to an improved representation of the PAC has been limited by a paucity of modeling approaches to mimic the multi-component architecture of the PAC region, and experimental data for validation.

In order to facilitate improved injury prediction, researchers may need to delve into tissue and cellular mechanics of the brain. Multiscale modeling or microstructure data integration into macroscale models of the head are common methods used to investigate TBI. [Cloots et al. \(2011, 2012, 2013\)](#) developed cellular, tissue, and whole-head FE models, and coupled them to determine how a multiscale modeling approach refined predictions of axonal injury. Inclusion of the cellular and tissue level details added important information to the model, but there were no experimental data to assess the influence of these nuances on predictions of axonal injury. [Wright et al. \(2013\)](#) used a different approach and implemented anisotropic behavior to elements within the white matter tract of the brain. The anisotropic behavior was based on a microscale model developed previously in their laboratory that utilized axonal tract direction data from diffusion tensor imaging ([Wright and Ramesh 2012](#)). Predictions of intracranial pressure and small brain strain in the finalized model were close to those reported from [Nahum and Smith \(1977\)](#) and [Sabet et al. \(2008\)](#), respectively, but validation of axonal injury prediction was not available. [Sullivan et al. \(2015\)](#) recently utilized an even simpler approach in that they developed a homogeneous model of the brain, but used DTI data to inform the direction of strain best capable of predicting axonal injury. Comparing predictions of axonal injury against animal experimental data, Sullivan et al. were able to show that this approach was capable of predicting axonal injury with 100 % sensitivity and 75 % specificity. Of note, the Sullivan et al. study is one of the few to actually test prediction capabilities against experimental data.

In terms of modeling more accurate interactions of the PAC, microscale modeling has been the dominant approach. A simple microscale model of the PAC was demonstrated by [Ma et al. \(2008\)](#) who modeled the PAC as a series of solid elements or beam elements sandwiched between two plates. No macroscale model was directly coupled with this

model, but they report that the overall mechanics of the microscale model with the solid elements better correlated with bovine PAC stress–strain data from tension and traction tests ([Jin et al. 2006, 2007a](#)). A second team developed a microscale model of the PAC based on anatomical drawings and paired it with a whole-head model to simulate head injury ([Zoghi-Moghadam and Sadegh 2009](#)). This model was an improvement over the state of the art, but their conclusions were limited due to the lack of available experimental data for validation. Additionally, the distribution of the microstructures was assumed to be uniform across the brain, but recent data shows that there is a large variation in the volume fraction of PAC arachnoid trabeculae throughout the brain (13.8–53.0 %) ([Scott and Coats 2015](#)).

In this study, we use multiscale models to identify how the anatomical variability of the PAC substructures alters cortical brain deformation, and potentially improves predictions of extra-axial hemorrhage (EAH) from non-impact head rotations. Using PAC anatomical and population density data (volume fractions of arachnoid trabeculae), multiple microscale FE models of the PAC were created to represent the natural mechanical variability of the PAC across the brain ([Scott and Coats 2015](#)). Representative solid elements (RSE) with transverse isotropic properties were created from simulations with the microscale model, and incorporated into a macroscale whole-head FE model previously developed by [Coats et al. \(2012\)](#). The effect of subject-specific PAC variability on brain–skull displacement and cortical stress distribution was evaluated, as well as the ability to predict regional EAH occurring from rapid, non-impact head rotations in a piglet model of TBI.

2 Methods

2.1 Microscale model geometry

The microscale PAC model consisted of a $1.5 \times 1.5 \text{ mm}^2$ section of PAC which included the upper-arachnoid membrane, arachnoid trabeculae (AT), subarachnoid vasculature, and pia membrane. The microscale PAC was constructed to represent the immature porcine anatomy and material properties as best as possible. Anatomical measurements were obtained for three structures: the upper arachnoid (UA), subarachnoid space (SAS), and subarachnoid vasculature (SAV). All dimensions were measured manually from optical coherence tomography (OCT) scans of two immature porcine postmortem brains which had their subarachnoid space filled with saline from a syringe pump at 8 mL/min ([Scott and Coats 2015](#)). This rate was the lowest rate possible to maintain a consistent pressurization of the subarachnoid space without damaging the structures or bursting the upper-arachnoid membranes, and was believed to be an adequate representa-

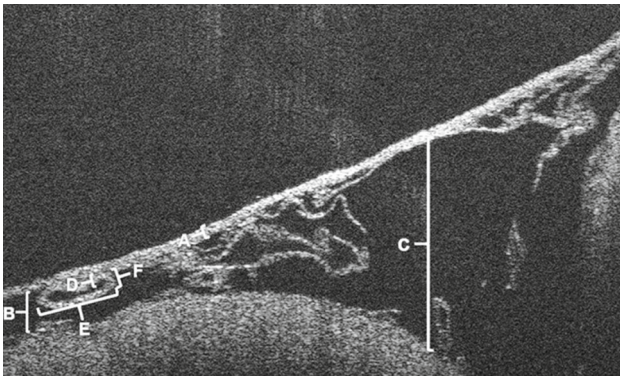


Fig. 1 Example OCT image with relevant measurements labeled: UA thickness (a), minimum SAS thickness (b), maximum SAS thickness (c), SAV lumen thickness (d), SAV major diameter (e), SAV minor diameter (f)

tion of an *in vivo* state for this study. The OCT scan windows were set at $1.5 \times 1.5 \times 2$ mm ($l \times w \times h$), which allowed for maximum in plane ($w \times h$) resolution (2×3.2 μm) while maintaining an adequate imaging window that captured multiple structures of the PAC (Scott and Coats 2015). This imaging window dictated the size of the microscale PAC model. Dimensions of all substructures were measured in a single representative 2D image from the middle of each 3D volumetric data set ($n=20$ for one brain and $n=27$ for the other). In our previous studies using OCT to characterize the microstructures of the PAC (Scott and Coats 2015), we reported that using a representative 2D image results in an error of no more than 10% of the 3D volume. This was deemed acceptable for our study.

UA thickness was measured in each 2D OCT image from both brains (Fig. 1a). The average \pm standard deviation was 27.06 ± 5.57 μm and 30 μm was selected for the microscale PAC model (Table 1). SAS thickness was measured in two locations from each OCT image. The first location was the “minimum” or smallest gap where AT structures were present. The second was the “maximum” or largest SAS gap where AT structures were present (Fig. 1b, c). Gaps were not measured where there were no AT structures, or where the pia extended below the image window (in the case of a deep sulcus). The average of these two measurements across all locations in both brains (287.92 ± 151.12 μm) was used to estimate an average SAS thickness of 300 μm for the PAC model, which assumed the UA and pia membranes were perfectly parallel.

The SAV in the OCT images were often collapsed and surrounded by a layer of arachnoid material. Therefore, the wall thickness and outer diameter of the SAV were estimated by scaling human measurements of cortical veins (Monson et al. 2005) by the ratio of human subarachnoid space reported in the literature (Armstrong et al. 2002; Frankel et al. 1998; Haggmann et al. 2011; Lam et al. 2001) to piglet sub-

Table 1 Dimensions of the microscale model of the immature piglet PAC

Structure	Parameter	Model dimension (μm)
Entire PAC	Slice area	1500×1500
	SAS thickness (Gap)	300
Pia membrane	Thickness	15
Arachnoid membrane	Thickness	30
Arachnoid trabeculae (AT)	Diameter of chords and sheet-end radii	18
	Length of short sheet	150
	Length of long sheet and sheet with SAV	450
Subarachnoid Vessels (SAV)	Outer diameter	112.5
	Wall thickness	18.75

arachnoid space as measured from the piglet OCT images. This resulted in an estimated SAV outer diameter of 112.5 and wall thickness of 18.75 μm . To verify that these estimates were reasonable, wall thickness and vessel diameter were measured in the OCT images (Fig. 1d). As mentioned, most vessels were not circular in the images, so the major and minor axes were measured and averaged to approximate a representative diameter (Fig. 1e, f). The average (\pm SD) wall thickness and vessel diameter in the images was 22.76 ± 6.86 μm and 183.74 ± 83.32 μm , respectively. The scaled measurements fall within one standard deviation of the average measured data, and were therefore deemed to be reasonable estimates. Measurements not directly measured from OCT images, such as pia membrane, were determined based on relative dimensions between substructures for other animals or species reported in the literature (Aimedieu and Grebe 2004; Jin et al. 2006, 2007b, 2011). Table 1 presents all dimensions of the microscale model.

In addition to the membranes, the microscale PAC model consisted of four basic AT substructures: a chord, a short sheet, a long sheet, and a sheet encompassing a subarachnoid vessel (Fig. 2a). These structures are placed between the pia and upper arachnoid. Because the focus of this study was of the overall mechanical behavior of the PAC, detailed anatomical morphology was not included. The simplified chord and sheet shapes were able to act as tethers between the upper and lower membranes in much the same way as the true anatomical structures do. CSF was excluded from the model. While this exclusion would have substantial implications during skull impact, it was felt that relative brain–skull displacement

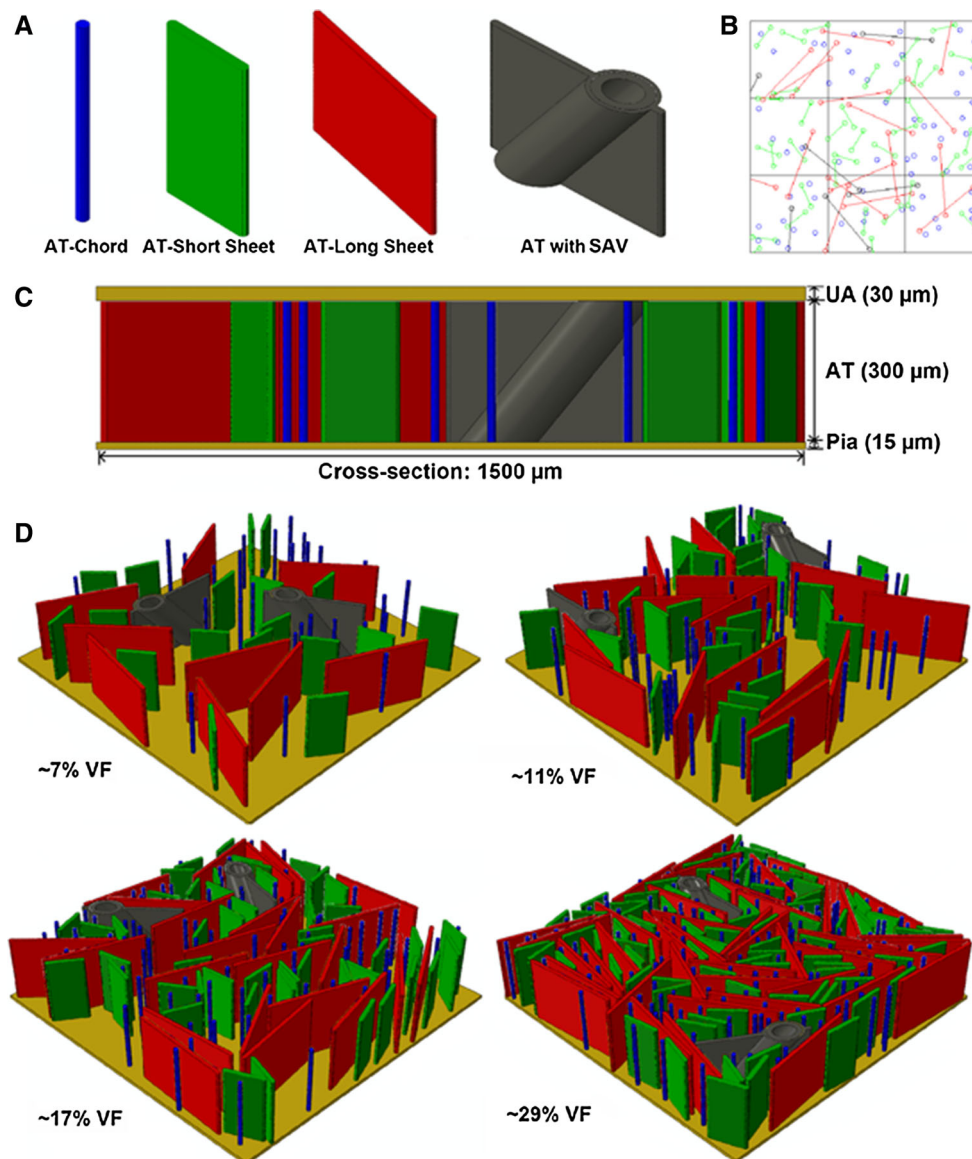


Fig. 2 Microscale model geometry. **a** Simplified arachnoid trabeculae structures. **b** Example of randomization algorithm output in a *top-down* view. **c** Final assembled model in a side-view. **d** Isometric views of the

PAC model with UA removed to show differing volume fractions (VF) of arachnoid trabeculae

during the rapid, non-impact head rotations investigated in this study would be minimally affected.

AT and SAV substructures were populated based on observations made during the OCT imaging studies. In general, more small spindly chord-like structures were observed than short and long sheets or SAV. As such, the PAC model was populated by defining a base set of component structures and multiplying this set to attain different total volume fractions. The base set of structures contained 10 AT chords, six AT short sheets, and three AT long sheets per set. This composition allowed the thinner, chord-like structures to dominate the model, and generally matched the observed ratio of structures during the OCT examinations. The average number of vessels

measured in all 47 OCT images was 1.35 (range 0–3 vessels). This average value did not drastically fluctuate for higher or lower volume fractions of AT. Therefore, the number of SAV structures was set to 2 for each model. Volumetric calculations were made by plugging the dimensions in Table 1 into basic geometric calculations for a cylinder (chord), cylinder+rectangle (sheets), and hollow cylinder (SAV).

Because the organization of the arachnoid trabeculae appeared arbitrary in the OCT images, substructure placement was randomized using a custom code written in MATLAB (2011b, The MathWorks Inc.). This script generated positions for the AT chord shapes by picking random values within the boundaries of the microscale model. Each time it

Table 2 Example calculation of volume fraction of the immature porcine microscale PAC model

Shape	Volume (mm ³)	No. of parts per base unit	Multiplier to create desired VF	Aggregate volume (mm ³)
Chord	7.634×10^{-5}	10	10	7.634×10^{-3}
Short sheet	8.863×10^{-4}	6	10	5.318×10^{-2}
Long sheet	2.506×10^{-3}	3	10	7.519×10^{-1}
Sheet /w/ SAV	5.074×10^{-3}	2	1 (not multiplied)	1.015×10^{-2}
Total volume of PAC				0.675
Ratio of aggregate AT volume divided by volume of PAC				$0.146/0.675 = 21.16\%$
Resulting Rounded VF				21%

Table 3 Final mesh parameters for the porcine microscale PAC model

Structure	Element type	Avg. aspect ratio	Avg. shape factor	Avg. edge length (μm)	Elements	Nodes	No. in model	Total nodes
AT Chord	C3D20R	1.79	n/a	4.46	848	4352	100	435,200
AT Short Sheet	C3D10	1.57	0.6894	9.07	15,758	25,480	60	1,528,800
AT Long Sheet	C3D10	1.8	0.6467	10.69	19,417	33,757	30	1,012,710
AT w-SAV	C3D10	1.43	0.7881	12.04	17480	31825	2	63,650
SAV	C3D20R	1.29	n/a	7.56	6336	32,164	2	64,328
Pia	C3D8R	3	n/a	10.00	30,000	40,804	1	40,804
UA	C3D8R	3	n/a	10.00	60,000	71,407	1	71,407
Total nodes in PAC model								3,255,562

chose a new point it tested that point's coordinates against previous points to ensure no intersection of substructures. After all chords were placed, the code then chose end points for sheet shapes. The code rotated each sheet shape by a random angle, thus randomizing any directionality in the sheets. The code generated a Python (v3.3.0, Python Software Foundation) macro which automated the model building process in ABAQUS (v6.12, Dassault Systèmes). A typical output of the MATLAB code is shown in Fig. 2b. The code does not account for overlap during the rotation stage (i.e. two sheets could cross each other like an "X"). While this overlap may physically occur in the PAC, identification of these types of structures from the OCT images was challenging. Therefore, all overlapping structures in our simulations were manually corrected in ABAQUS to simplify meshing and geometry. Figure 2c shows the final geometry of the model and Fig. 2d showcases some representations of the different VF microscale models created for this study. Table 2 presents an example of the VF calculation for the 21% VF model.

2.2 Microscale model meshing

The meshing of the PAC model was informed by a previously conducted convergence study on a previous model for the

human (Scott 2014). Aside from its relative size (the human PAC model was larger than the current porcine PAC model), both models have the same aspect ratios and geometry. The mesh element types were all kept the same as the human model. The element edge length was scaled down by creating equidistant edge seeds on the ends of the chords and sheets and propagating them uniformly through the structures. This resulted in roughly the same number of nodes. Table 3 presents the final mesh parameters for the 21% VF model and Fig. 3 provides a visual of each meshed part.

2.3 Microscale model material properties

Material data for the PAC is limited to a series of bovine studies performed by Jin et al. in tension (2006), normal traction (2007a, 2007b), and shear (2011). In tension, the pia and UA membranes are being uniaxially loaded while the AT structures likely contribute very little to the response. Therefore, the data reported from these tests were assumed to be representative of moduli for the pia and arachnoid membranes. The results in Jin et al. showed a strain rate-dependent "bilinear" response (a linear toe region, followed by a stiffer linear working range). The stiffer, high strain modulus from the highest strain rate test (15.8 MPa) was used in this study.

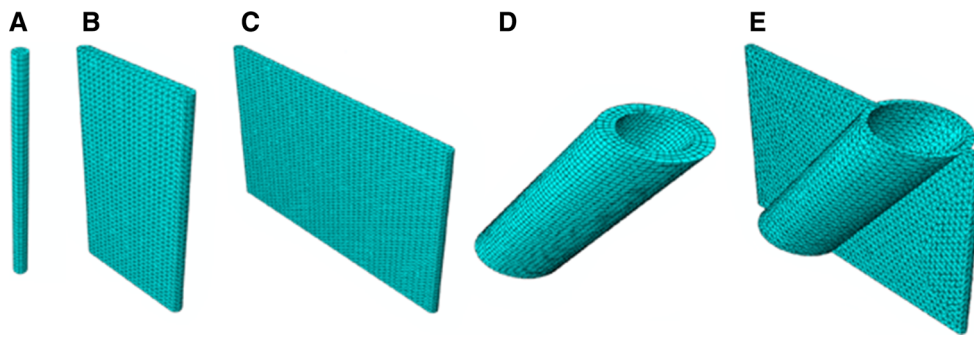


Fig. 3 Final meshes for microscale PAC model: **a** AT chord, **b** AT short sheet, **c** AT long sheet, **d** SAV, **e** SAV-enveloping AT sheet

Table 4 Material properties utilized in microscale model of porcine PAC

Structure	Modulus (E)	Source
AT structures	284.8 kPa	(Jin et al. 2007b)
SAV	27.3 kPa	(Pang et al. 2001)
Pia & UA	15.8 MPa	(Jin et al. 2006)

Density was assumed to be 1130 kg/m^3 and Poisson's ratio to be 0.45

The normal traction tests conducted by Jin et al. (2007a, b), applied tensile force normal to the surface of the brain, and thus passed most of the load to the AT structures. These tests exhibited a linear elastic response, so the AT were assumed to behave similarly. In the calculation of stress, Jin et al. divided their measured loads by the cross-sectional area of the entire rectangular PAC specimen, thus reporting an effective elastic modulus of the entire structure. To estimate the elastic modulus of a single AT, the volume fraction of AT present in the Jin et al. studies was assumed to be equivalent to the average volume fraction from our OCT measurements (21 % VF) and the remainder of the space void or negligible. The effective modulus (59.8 kPa) was scaled up by the inverse of the volume fraction resulting in a single AT elastic modulus estimate of 284.8 kPa.

The elastic modulus of the SAV was estimated from porcine cerebral bridging vein stress–strain data tested in the longitudinal direction (Pang et al. 2001). Density and Poisson's ratio were assumed to be 1130 kg/m^3 and 0.45, respectively (Barber et al. 1970). Table 4 presents the material properties used for all structures in this study.

2.4 Development of PAC representative solid element material properties

In order to implement the microscale model's behavior into the macroscale model, solid elements with material properties representative of the different volume fractions were created for each PAC model. The material behavior of the PAC representative solid element (RSE) was dictated by sim-

ulating uniaxial tensile tests parallel and perpendicular to the meninges of the microscale model, similar to the material tests conducted by Jin et al. (2006, 2007b). The tensile test simulations parallel to the meninges were conducted by fixing the pia and UA on one side, and applying a prescribed displacement to the other end (Fig. 4a). This prescribed displacement was 0.225 mm, which resulted in 15 % strain. This resulted in a moderate value of extension but did not exceed the level of strain that the weakest samples failed at in Jin et al.'s studies. The reaction force was collected and divided by the cross-sectional area of the pia and UA to calculate the stress response of the simulated material test. The cross-sectional area was calculated from the pia and UA only (i.e. not including the SAS) because the load in these simulations is carried almost entirely by the pia and UA.

The normal traction test simulations (i.e., tension perpendicular to the meninges) were conducted by fixing the bottom surface of the pia and prescribing a displacement of 0.15 mm to the top surface of the UA (Fig. 4b). This displacement resulted in a 50 % strain of the 0.300 mm tall AT structures and represented a moderate level of stretch without going above the failure points of the weakest tests reported by Jin et al. (2007b). The reaction force was divided by the top surface area of the arachnoid membrane to calculate stress.

The stress–strain responses of the microscale test simulations were plotted to visualize trends with volume fraction. The tensile tests were largely dominated by the pia and UA, and VF did not influence the results (Fig. 5a). However, large differences were seen in the traction test simulations with different VF (Fig. 5b). This was expected because the AT dominates the material response for these normal traction tests.

Several tests were conducted to see if any bias was introduced into the PAC models from the randomization procedure. For this assessment, the lowest VF model (7 %, which had the least AT structures and would be most influenced by directionality of such structures) was tested in both in-plane directions (x and y). A second model was built with a new randomized set of structures, still with a 7 % VF. This model was also subjected to tensile tests in two in-plane directions. The results of these tests showed no significant differences,

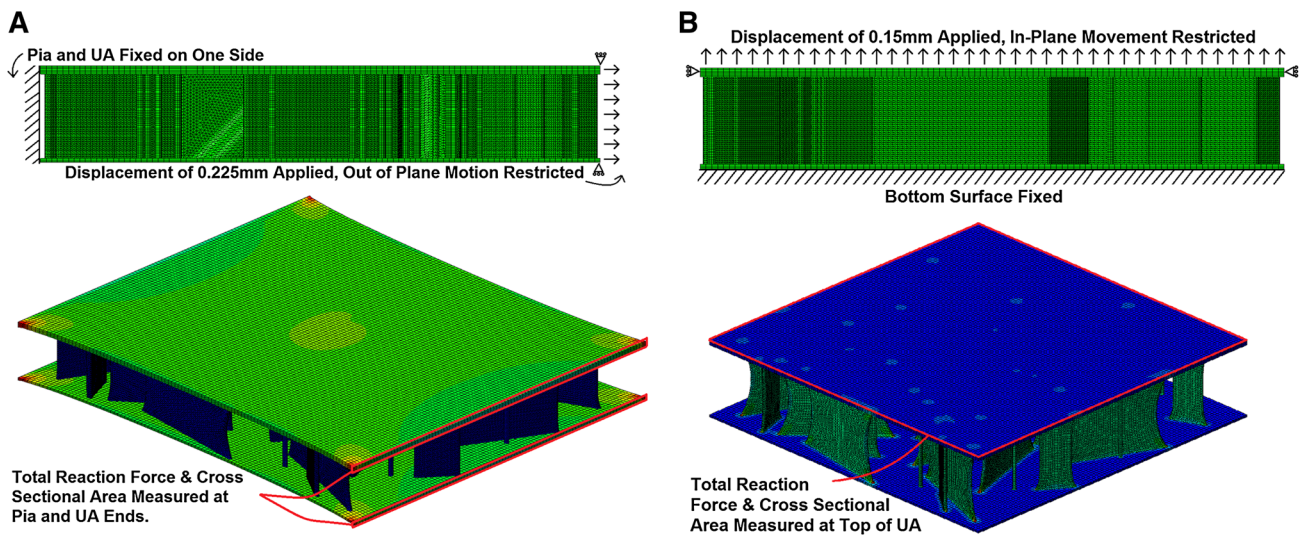
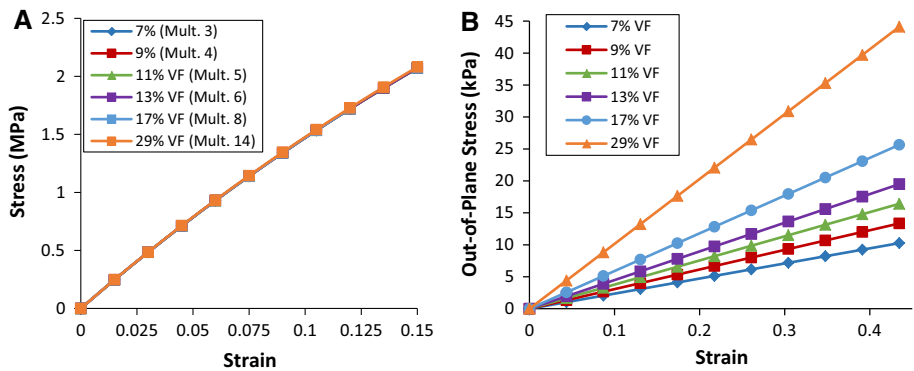


Fig. 4 Boundary conditions and loading for the tensile (a) and normal traction (b) test simulations. Post-deformation stress maps showcase the surfaces used to collect reaction force and cross-sectional area in calculations of stress in the RSE

Fig. 5 Stress–strain curves for all VFs for (a) tension simulations (uniaxial loading along the pia and arachnoid membranes) and (b) traction simulations (tension normal to the surface of the brain). Tension simulation results were independent of volume fraction while traction simulation results varied linearly with volume fraction



with a maximum error of 0.006 % occurring at the maximum stress point.

Each stress–strain curve from the test simulations was fit to a linear regression trend line, and the resulting linear slope in the regression equation was used as the modulus (Fig. 5). Each modulus was then plotted against its corresponding VF for the two types of tests (Fig. 6). For the tensile test simulations, there appeared to be a slight increase in stiffness of the RSE for increased VF and some small nonlinearity. However, the variation over the VF range was very small ($\leq 0.4\%$; Fig. 6a). Therefore, an average of all of the moduli was chosen to represent the isotropic in-plane linear elastic response. The moduli from the traction simulations were directly proportional to the change in VF, so this linear relationship was used to determine the out-of-plane linear elastic response for the RSE of volume fractions not simulated.

The RSEs were implemented into the macroscale model as transversely isotropic elements. The reported in-plane modulus (E_P) and out-of-plane, or transverse, modulus (E_T) had to be supplemented with data from the literature, as well as by using classical mechanics relationships, in order to form

a complete material model which included the in-plane Poisson’s ratio (ν_P), transverse Poisson’s ratio (ν_{TP}), in-plane shear modulus (G_P), and transverse shear modulus (G_{TP}). Note that for the differing VF models, only the transverse modulus (E_T) and transverse Poisson’s ratio (ν_{TP}) were varied (Table 5). All other values were kept constant (Table 6) based on the assumptions and equations detailed below.

The in-plane Poisson’s ratio would be almost entirely governed by the pia and UA moduli, but no literature exists which reports this value. Persson et al. (2010) report the Poisson’s ratio for spinal dura, which can be compared to cranial dura if one considers the circumferential direction measurements (the longitudinal measurements contain much higher collagen fiber directionality than cranial dura). Based on these reported data, the estimated in-plane Poisson’s ratio was 0.45.

The transverse Poisson’s ratio was calculated based on the ratio of the in-plane and transverse moduli recommended by ABAQUS to ensure model stability (Eq. 1).

$$\nu_{TP} \leq \left(\frac{E_T}{E_P} \right)^{1/2} \tag{1}$$

Fig. 6 Elastic moduli determined from the microscale PAC model simulations of tension (a) and normal traction (b) tests. In-plane modulus was not substantially influenced by PAC volume fraction in tension simulations, but out-of-plane modulus increased linearly with volume fraction in traction test simulations. A y intercept of 0 was enforced for normal traction tests

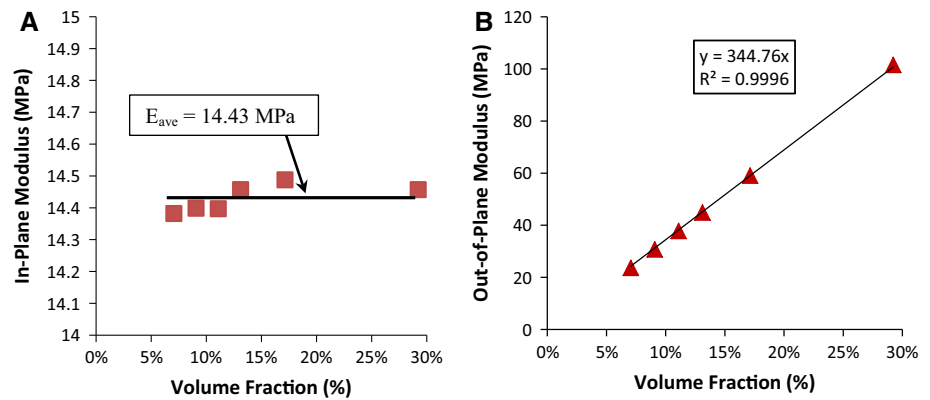


Table 5 Transverse modulus and transverse Poisson's ratio for the RSEs across a range of VFs

VF (%)	E_T (kPa)	ν_{TP}	VF (%)	E_T (kPa)	ν_{TP}
7	24.40	0.000761	25	87.07	0.002715
9	31.36	0.000978	27	94.03	0.002932
11	38.32	0.001195	29	100.10	0.003150
13	45.29	0.001412	31	107.96	0.003367
15	52.25	0.001629	33	114.92	0.003584
17	59.22	0.001847	35	121.89	0.003801
19	66.18	0.002064	37	128.85	0.004018
21	73.14	0.002281	39	135.81	0.004235
23	80.11	0.002498	41	142.78	0.004452

Table 6 Constant material properties for all RSEs regardless of VF

Property	Value
In-plane modulus (E_P)	14.48 MPa
In-plane Poisson's ratio (ν_P)	0.45
In-plane shear modulus (G_P)	4.98 MPa
Transverse shear modulus (G_{TP})	22.37 kPa

This calculation resulted in very low values of ν_{TP} (Table 5). Physically this makes sense as stretching or compressing the AT would likely result in minimal strains to the pia and UA.

The in-plane shear modulus (G_P) was calculated based on the classical mechanics relation between shear modulus, elastic modulus, and Poisson's ratio (Eq. 2). The in-plane elastic modulus (14.43 MPa) and assumed in-plane Poisson's ratio of 0.45 were utilized because the pia and UA largely dominate this shear response.

$$G_P = \frac{E_P}{2(1 + \nu_P)} = \frac{14.43 \text{ MPa}}{2(1 + 0.45)} = 4.98 \text{ MPa} \quad (2)$$

The transverse shear modulus (G_{TP}) was extracted from PAC shear tests performed by Jin et al. (2011) at different strain rates. The modulus from the highest strain rate test (22.37 kPa) was selected.

2.5 Macroscale porcine model parameters

The macroscale model utilized in this study is one that has already been verified and validated in an FE study on non-impact rapid head rotations in the immature piglet by Coats et al. (2012). The geometry was created by segmenting a sequence of coronal computed tomography (CT) images of a 4-week-old pig brain, and scaling the dimension of that brain to that of an average 3- to 5-day-old piglet brain (Fig. 7). The skull geometry was created by extending the brain's free surface outwards by 1 mm, and smoothing to remove gyral morphology. The skull was represented with rigid elements because only non-impact rotations were simulated and the pediatric skull is orders of magnitude stiffer than the brain and PAC (Coats and Margulies 2006a, b; Jin et al. 2007b). The falx was created based on measurements obtained in-house with calipers in-vivo and ex-vivo. The model consisted of 17,587 elements (13,018 brain and brainstem hexahedral elements, 1891 falx tetrahedral elements, and 2678 skull rigid elements).

The material properties of the previously published model represent a 3- to 5-day-old piglet. The brain is character-

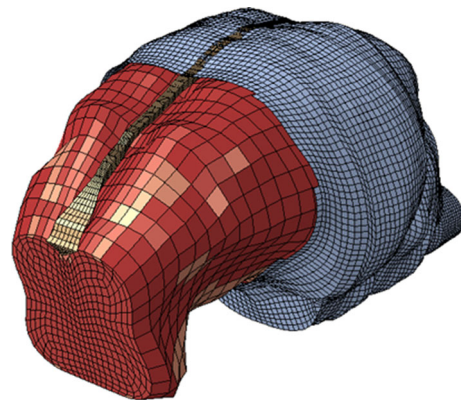


Fig. 7 Macroscale finite element model of a 3- to 5-day-old piglet brain and skull. Components include brain (red), brainstem, falx (brown), and skull (blue). A portion of the skull (blue) has been removed to illustrate the underlying falx and brain

Table 7 Material properties utilized in the macroscale whole head model

Structure	Material property
Brain/brainstem	$\mu = 526.9 \text{ Pa}$ $\tau_1 = 2.96 \text{ s}$ $\alpha = 0.01$ $\tau_2 = 0.181 \text{ s}$ $C1 = 0.332$ $\nu = 0.49999$ $C2 = 0.389$
Falx	$\rho = 1.13 \text{ g/cm}^3$ $E = 16 \text{ MPa}$ $\nu = 0.45$
Skull	Rigid Body

ized as nonlinear homogenous, isotropic hyperelastic and viscoelastic using a first-order Ogden strain energy equation. The model parameters were determined from data presented on samples from 5-day-old piglets and have been published previously (Prange and Margulies 2002). The falx was represented as linear elastic with material properties scaled down from Galford and McElhaney's reported adult values (1970), based on a ratio of adult to fetal dural stiffness calculated from data by Bylski et al. (1986). Table 7 presents a summary of all of the material properties utilized in the macroscale model.

2.6 Implementing a representative solid element into macroscale models

The previous Coats et al. model utilized linear elastic connectors to define the interaction between the brain and the skull. These connectors represented the tethering provided by the cortical vasculature and were modeled using the material properties of cortical veins from autopsy by Monson et al. (2005). For the VF models, these connectors were removed and 2678 solid hexahedral RSEs were added between the brain and the skull to represent the PAC. The separation between the brain and skull in the previous model was 1 mm, which caused the RSEs in this model to be 1 mm thick as well. The in-plane edge lengths were determined from the meshing scheme used previously by Coats et al. (2012) and were 1.5–2.5 mm.

The RSE elements were isolated and segmented into the 12 regions that were scanned in previous OCT imaging studies (Scott and Coats 2015). These 12 regions represent the groupings created when splitting the brain into left and right hemispheres, medial and lateral to midline, within frontal, parietal, and occipital lobes (Fig. 8). A 13th region was created that represented all non-scanned regions (NSR). Each of the 12 scanned regions was populated with the material properties of the RSE that represented the average VF found in that region.

Two macroscopic models were created to represent the VF data from two different animals. These two models are

referred to as “High-VF” and “Low-VF” models because they represent the animals with the highest and lowest average volume fractions reported in our previous imaging study. The average volume fraction of the PAC across the entire brain differed by 5% between the two animals. The regional volume fractions (as pictured in Fig. 8 and labeled as sub-region in Table 8) differed by as little as 0.6% (in the left lateral parietal region), and as much as 15% (in the left lateral frontal region) between the animals. Figure 9 presents the distribution of volume fraction measurements across the two brains. Table 8 provides the averages of the 12 sub-regions used to populate the FE models. The unscanned region of both models was populated with RSE's representing the overall average VF for each animal.

The material model of all RSE elements was transversely isotropic, linear elastic. The in-plane directions (the two directions with identical moduli) were the two directions tangent to the brain's surface, dictated by the pia and UA's response. The out-of-plane direction was perpendicular to the brain's surface (dictated by the AT response). To properly apply transverse isotropy, a local coordinate system was established in ABAQUS, in which the z direction (out-of-plane) for each element was perpendicular to the brain's surface.

2.7 Macroscale model loading

The low and high-VF macroscale models were each subjected to 24 angular velocity profiles extracted from rapid non-impact piglet head rotation experiments reported by Eucker et al. (2011) and used by Coats et al. (2012). These axial, coronal, and sagittal head rotations employed angular accelerations of 26 to 85 krad/s^2 and angular velocities of 130–220 rad/s , and produced a range of traumatic brain injury etiologies including diffuse axonal injury and bilateral extra-axial hemorrhage (consisting of subdural and subarachnoid hemorrhage) in the more severe cases. A summary of all the simulations completed by both the low- and high-VF models is provided in Table 9.

2.8 Macroscale model post-processing

To compare differences between the low- and high-VF models, we compared the population distribution of brain–skull displacement. To calculate relative displacement, the coordinates of all the outer surface nodes of the brain and inner surface nodes of the skull were extracted at all time-points (every 0.1 ms) and closest node pairs were identified. These node sets were imported into a MATLAB code which subtracted the values of the skull's displacement from the values of the brain's displacement for each adjacent node pair. Peak brain–skull displacement distribution plots were created for five regions within the model which mimicked the five

Fig. 8 RSE element assignment to the whole-head model. The 1st letter indicates left or right, 2nd letter indicates medial or lateral, and 3rd letter indicates frontal, parietal, or occipital. NSR indicates the non-scanned region

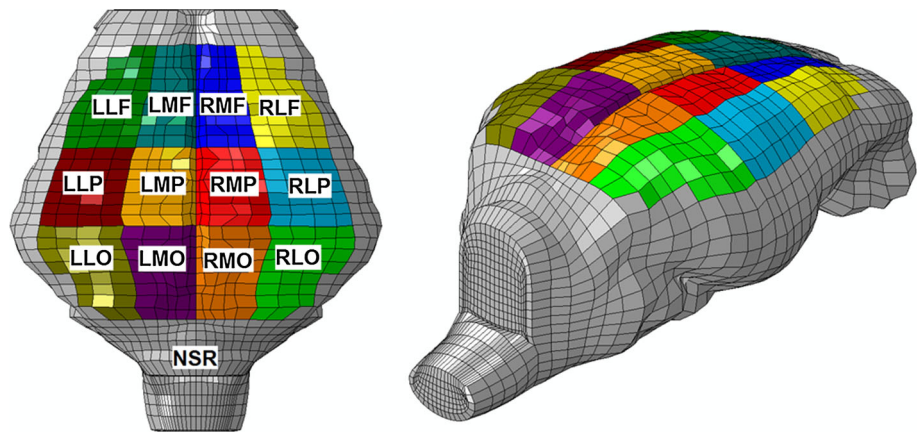


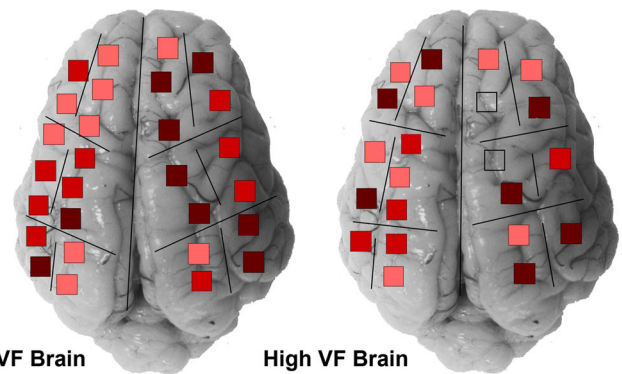
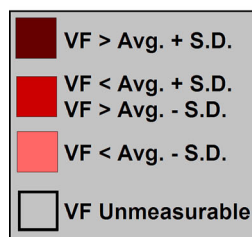
Table 8 Average VF values for each anatomical subregion of the two inflated brains

Subregion	Low-VF model (%)	High-VF model (%)
LLF	14.1±6.5	29.1±13.6
LLP	17.2±3.6	16.6*
LLO	23.1±5.2	37.2±11.0
LMF	11.0±2.7	24.1±18.1
LMP	22.0±5.0	23.1±7.6
LMO	15.1±1.1	20.4±5.6
RLF	29.2±10.4	24.4±13.2
RLP	18.9±0.5	26.3*
RLO	26.3±2.4	34.79*
RMF	22.7±8.3	11.2*
RMP	33.3±12.0	32.8*
RMO	15.0±7.9	27.8±15.5
Entire Brain Average (±S.D.)	20.29 (±7.96)	25.83 (±10.26)

1st letter indicates left or right, 2nd letter indicates medial or lateral, and 3rd letter indicates frontal, parietal, or occipital

* Only one area imaged per region

Fig. 9 Color map of VF distributions in each of the two brains with boundary lines indicating the defined regions in Fig. 8. Averages and standard deviations are calculated for each brain from the last row in Table 8. Note that positions are approximate and based on notes collected from the operator during the imaging session



regions used to categorize intracranial hemorrhage prediction (IHP) scores in previously published animal experiments (Coats et al. 2012).

Coats et al. (2012) reported that cortical principal stress was a good predictor of extra-axial hemorrhage when the model contained solid elements for the PAC. Therefore, the maximum principal stress for the elements on the brain's sur-

face was also extracted from the low- and high-VF models, and plotted in a similar manner to the brain-skull displacement. Significant differences between the distribution plots of each animal for each region were evaluated with a two-sample Kolmogorov-Smirnov goodness-of-fit test for continuous distributions. A p value < 0.05 was used to indicate statistically significant differences between the dis-

Table 9 Summary of simulation matrix

	Plane of rotation	Angular velocity (rad/s)	IHP Scores				Midline (%)	Total (%)
			Anterior left (%)	Anterior right (%)	Posterior left (%)	Posterior right (%)		
1	Axial	200.6	65	43	35	6	51	37
2	Axial	202.9	64	68	18	47	35	44
3	Axial	210.9	18	27	13	16	39	19
4	Axial	179.0	60	59	30	22	42	39
5	Axial	183.9	25	29	8	11	29	18
6*	Axial	199.2	49	51	13	47	68	40
7*	Axial	181.3	22	33	11	7	43	19
8*	Axial	161.5	1	3	14	12	20	10
9	Axial	197.9	44	17	31	21	58	31
10*	Axial	168.6	23	9	8	5	30	12
11	Axial	169.9	44	33	17	14	53	27
12	Axial	194.7	34	39	16	13	50	26
13*	Axial	144.0	0	0	0	4	1	1
14*	Axial	130.8	0	1	0	0	0	0
15	Axial	165.1	17	21	2	7	4	9
16	Coronal	217.7	0	1	1	2	0	1
17	Coronal	193.4	0	0	0	1	0	0
18	Coronal	214.6	1	1	5	0	0	2
19	Coronal	196.0	0	0	0	0	0	0
20	Coronal	169.5	0	0	1	0	0	0
21	Coronal	207.8	0	0	0	0	0	0
22	Sagittal	160.4	15	14	19	17	67	20
23	Sagittal	156.7	28	31	23	23	94	32
24	Sagittal	161.3	27	25	25	11	66	25

The low-VF model and the high-VF model were used to simulate all of these experimental studies encompassing a range of angular velocities, head rotation directions, and severities of injury

* Simulations used to develop injury thresholds. Remaining simulations were used to evaluate the predictability of the threshold

tributions. A two-way ANOVA with a Tukey-Kramer post hoc analysis was used to determine significant differences in peak brain–skull displacement and principal cortical stress with direction of head rotation and region.

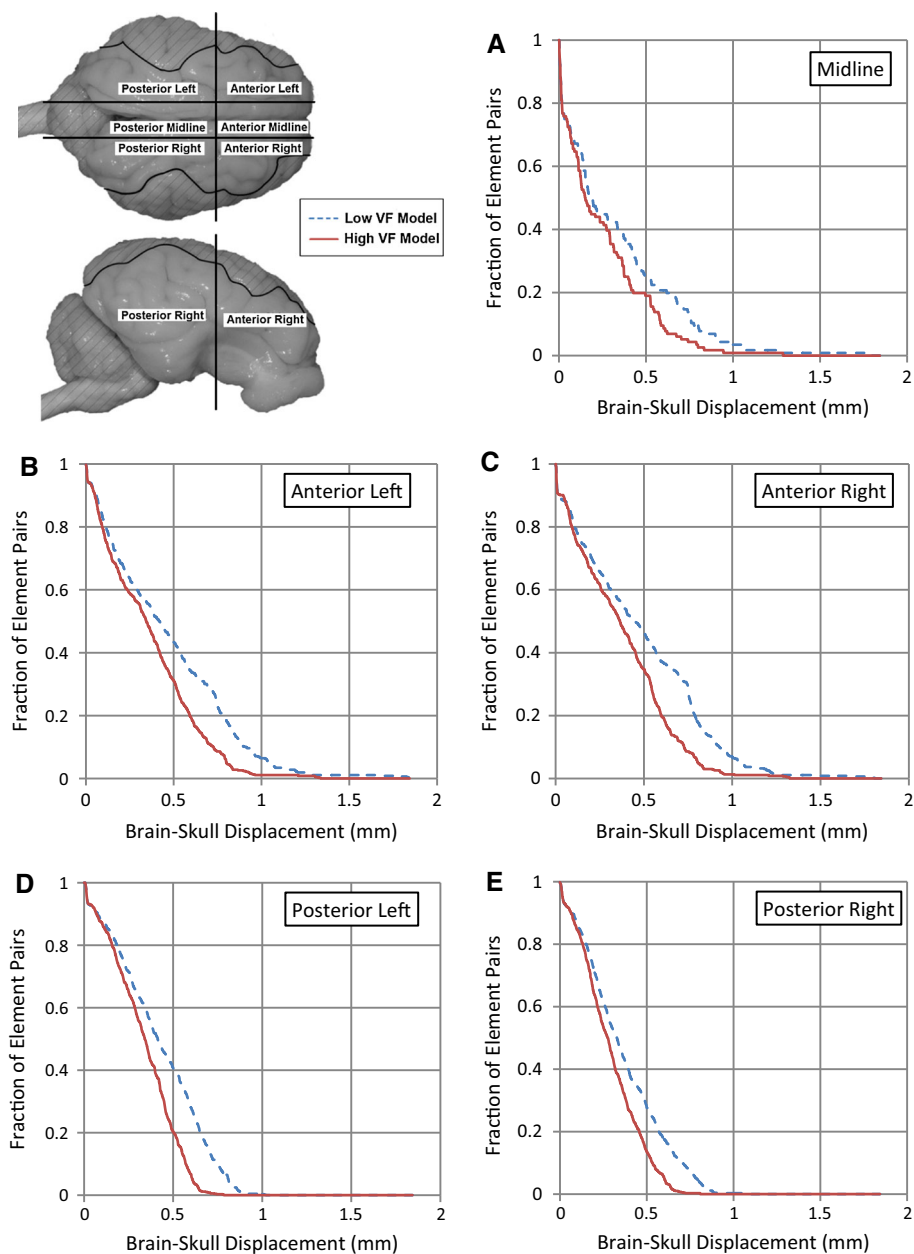
Results from simulations using the low- and high-VF models were also compared with results from the previously described macroscale simulations representing the PAC with uniform elastic connectors. Coats et al. defined positive intracranial hemorrhage in the animal experiments as any of the five regions of the brain with $\geq 25\%$ of the region covered in blood. This value is called the IHP cutoff percentage. Using a receiver operating characteristic (ROC) methods, the top 1% of peak connector strain was determined to be the optimal predictor, with 0.31 mm/mm as the connector strain threshold for predicting EAH.

To determine the optimal EAH predictor for the VF models, simulation and IHP data from six of the 24 animals were

input into a MATLAB code which evaluated different combinations of IHP cutoff percentage and prediction threshold for brain–skull displacement and principal stress prediction metrics. These six animals were selected because they represented a range of velocities and injuries in the axial plane of rotation. ROC curves were generated for each combination of IHP cutoff percentage and prediction threshold for each metric. The combinations with the highest area under the ROC curve were then evaluated individually for sensitivity and specificity according to different metric thresholds. The final choice on which combination to use was based not only on a large area under the ROC curve, but also on exhibiting an even balance of high sensitivity and specificity. This process was performed for the low-VF and high-VF models separately.

Once the final IHP cutoff percentage, prediction metric, and associated injury prediction threshold value were identi-

Fig. 10 Brain–skull displacement distribution curves for five IHP analysis regions [midline (a), anterior left (b), anterior right (c), posterior left (d), posterior right (e)]. The low-VF model consistently resulted in significantly higher brain–skull displacements



fied, a sensitivity and specificity analysis was used to evaluate how the macroscale model predicted regional and overall hemorrhage in the remaining 18 animals not used in the development of the prediction metrics.

3 Results

3.1 Comparison of two subject-specific multiscale models

The Kolmogorov–Smirnov goodness-of-fit tests resulted in p values of < 0.0001 for all five regions, indicating that the brain–skull displacement distributions predicted by the high-

and low-VF models were significantly different (Fig. 10; Table 10). As might be expected, the brain–skull displacement for the low-volume-fraction model was greater overall than the high-volume-fraction model, and the maximum brain–skull displacement differed by 0.15–0.29 mm (7–28%) between the models (the greatest discrepancies of roughly 0.29 mm occurred in the posterior left and right regions). The cortical stress was less affected by the differences between the low- and high-VF models and differed by 1–10%, except in the posterior right region which differed by 16% (21.35 kPa). These differences were driven primarily by the axial and sagittal head rotation simulations as there were minimal differences found between the models when simulating coronal head rotation.

Table 10 Average \pm standard deviation (maximum) of peak brain–skull displacement and maximum cortical principal stress for the low-VF and high-VF models

	Displacement (mm)		Cortical Stress (kPa)	
	Low VF	High VF	Low VF	High VF
Anterior Left	0.7480 \pm 0.5250 (2.2195)	0.6064 \pm 0.4525 (2.0309)	93.34 \pm 42.73 (165.62)	88.84 \pm 38.53 (155.54)
Anterior Right	0.7642 \pm 0.5175 (2.1808)	0.6145 \pm 0.4503 (2.0337)	90.15 \pm 36.65 (150.19)	90.17 \pm 37.03 (151.67)
Posterior Left	0.8339 \pm 0.2702 (1.3094)	0.6875 \pm 0.1956 (1.0215)	95.14 \pm 44.20 (171.20)	86.39 \pm 38.71 (156.17)
Posterior Right	0.8023 \pm 0.2953 (1.3365)	0.6193 \pm 0.2247 (1.0489)	90.03 \pm 34.19 (151.89)	83.01 \pm 30.99 (130.54)
Midline	0.8677 \pm 0.5148 (2.1772)	0.6751 \pm 0.4202 (2.0102)	83.37 \pm 34.14 (134.23)	77.92 \pm 33.96 (139.52)

3.2 Differences with head rotation direction

For both the low- and high-VF models, the magnitudes of maximum brain–skull displacements and cortical stresses were significantly dependent on the direction of head rotation. Simulations of sagittal head rotation resulted in significantly higher magnitudes of brain–skull displacement and cortical principal stress than axial head rotations, which were significantly higher than coronal head rotations ($p < 0.001$; Fig. 11). Sagittal head rotations exhibited near-perfect left/right anterior lobe symmetry for brain–skull displacement, despite differing RSE elements for the left and right hemispheres of the brain. Principal cortical stress during sagittal head rotations did not exhibit the same degree of symmetry.

Maximum values of brain–skull displacement were also significantly dependent on region and the interaction between head rotation direction and region ($p < 0.0001$). Average maximum brain–skull displacements following sagittal head rotation were largest in the anterior left/right and midline regions (2.047 ± 0.177) and more than double maximum brain–skull displacements in the same regions from axial (0.661 ± 0.236) and coronal (0.513 ± 0.114) head rotations. Maximum values of principal cortical stress were only significantly dependent on the direction of head rotation. Average maximum values of principal cortical stress from sagittal (125.62 ± 17.1) and axial (103.87 ± 27.73) head rotations were nearly three times greater than maximum principal cortical stress resulting from coronal head rotations (39.12 ± 6.80), regardless of region.

3.3 Comparison of multiscale model to previous connector model

The multiscale simulations exhibited stress patterns with smaller, localized hot spots of stress than the connector model. The connector model has homogenous stress contours due to the homogenous nature of the spring connectors. Two major kinematic events were observed to create local peaks

of stress. The first is when the skull is leading the brain and the PAC is in tension (Fig. 12). This occurs at the same time for the multiscale models, but slightly earlier for the connector model. At this time point, there is a large concentration of stress in the midline regions of the multiscale models with some “fingers” of stress across various regions of the brain due to the variability in the PAC elements. In the connector model, there is only one large concentration of stress that spans the occipital and parietal lobes. The second major kinematic event is when the brain “catches up” to the skull and is now leading, causing compression of the PAC elements (bottom row of Fig. 12). During this stage, there is a hot spot of stress in the midline at the intersection of the frontal and parietal lobes in the multiscale models, but there is a much higher level of stress and more discontinuity in the connector model. The more localized stress patterns in the multiscale model were observable in all three of the head rotation directions (i.e., sagittal, coronal, or axial).

3.4 Hemorrhage prediction abilities of the new model

Based on the receiver operating characteristic curves developed from the simulations of six of the 24 animal experiments, the brain–skull displacement or cortical principal stress experienced by the top 5% of the nodes or elements, respectively, was found to be the best predictor of intracranial hemorrhage for each metric. The low- and high-VF models had brain–skull displacement thresholds of 0.373 and 0.284 mm, respectively (Fig. 13). The cortical stress thresholds were 46.6 and 44.7 kPa for the low- and high-VF models, respectively. Despite these differences in thresholds, the overall sensitivities and specificities of the predictions were fairly consistent between the low- and high-VF models, especially when cortical stress was used as a predictor. Of note, the two VF models were generally more sensitive to predictions of hemorrhage than the previously published connector model (Coats et al. 2012), because only 1% of each region of the brain had to be covered in blood in order to detect the hemorrhage in the animal experiments. This is

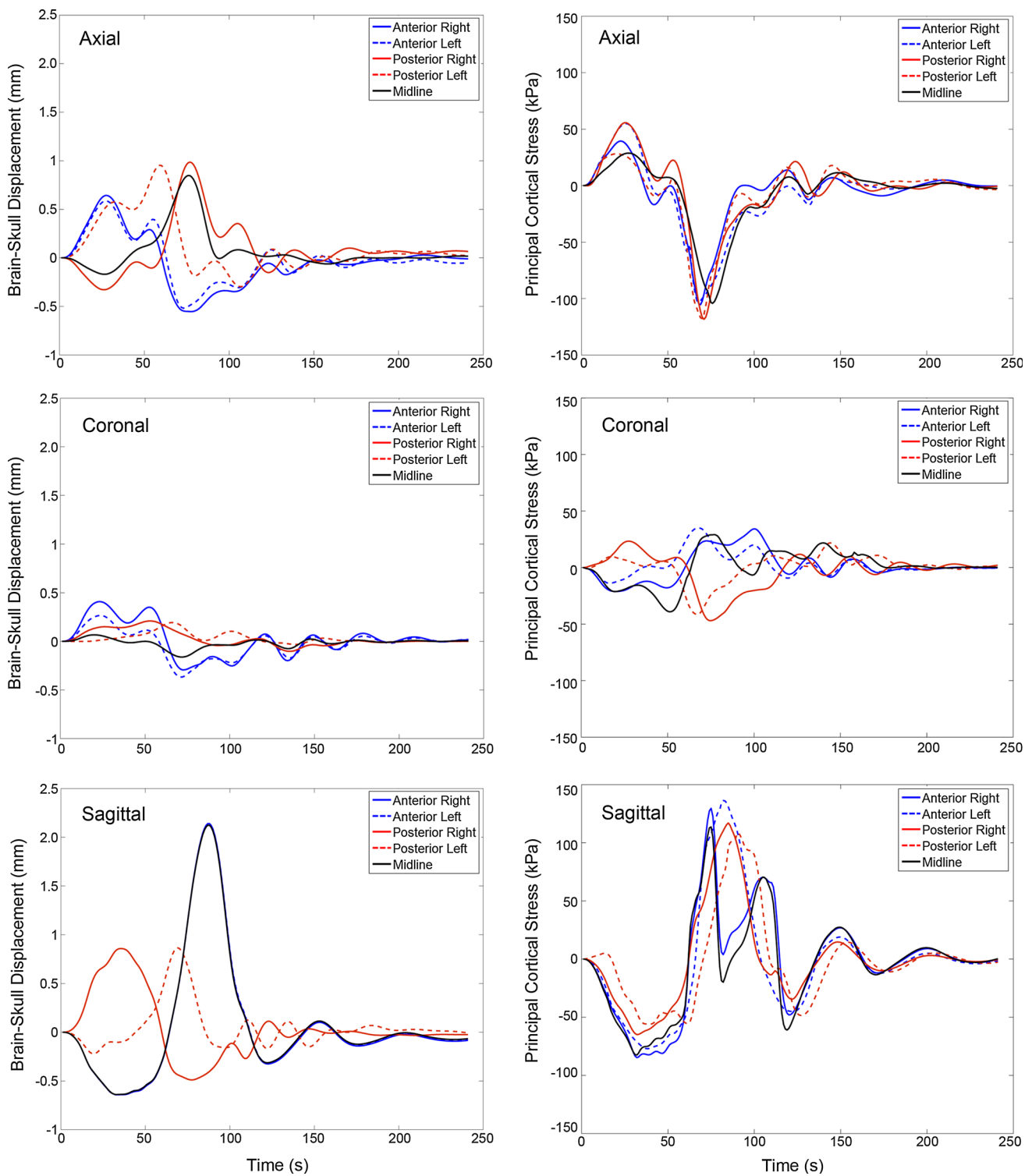


Fig. 11 Regional time history of the maximum node pair brain–skull displacement and principal cortical stress for a single representative animal simulation with axial, coronal, and sagittal head rotation. Note that the same animal model was used for each representative direction, but

the location at which the maximum node pair brain–skull displacement and maximum principal cortical stress occurred were not necessarily the same

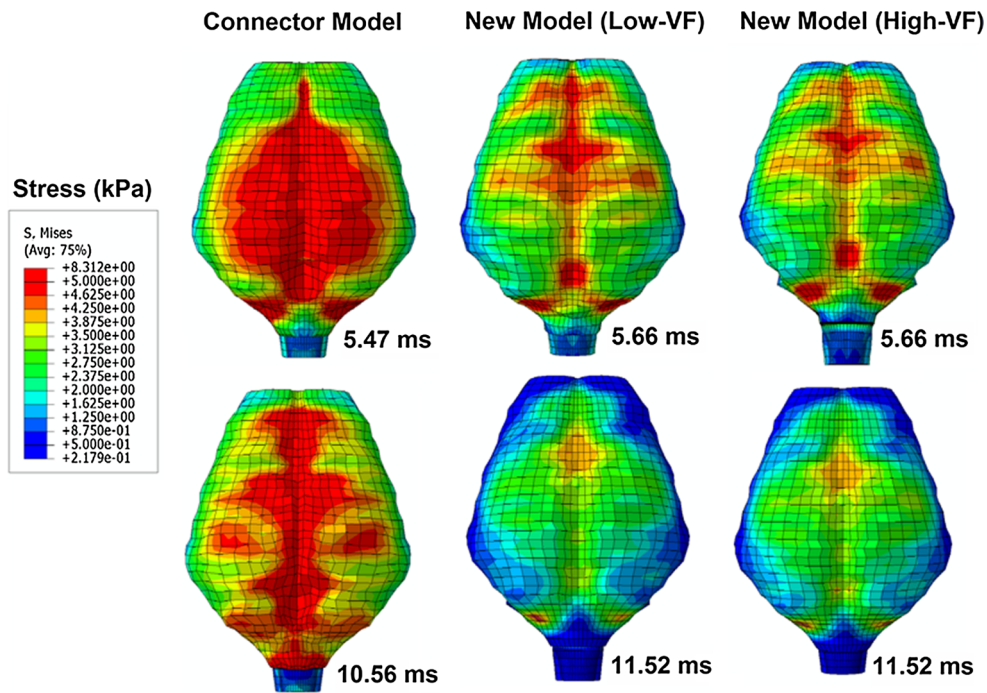


Fig. 12 Stress maps of the top surface of the brain at the times of highest stress in a simulation of the same sagittal head rotation using the three different PAC models. In the *top row*, the skull is leading the

brain and the PAC is in tension. In the *bottom row* the brain has caught up with the skull motion. The brain is now leading and the PAC is in compression

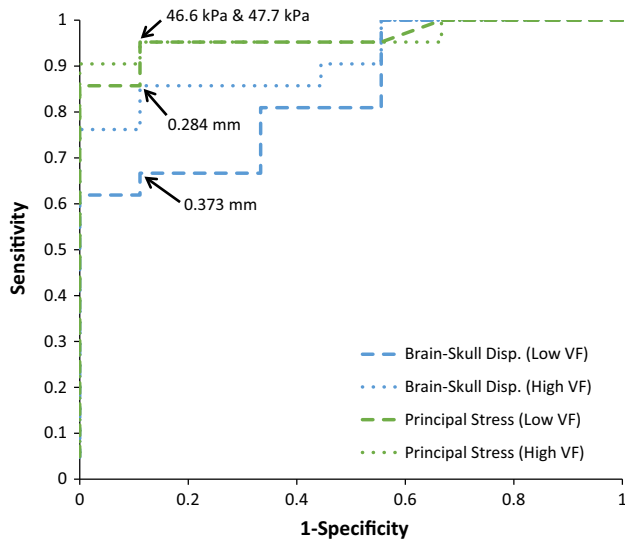


Fig. 13 ROC Curves for each of the best predictors of hemorrhage. Arrows indicate the exact point on the curve which represents the FE metric threshold value chosen. Note that the cutoff values for the stress analyses of the low- and high-VF models occupy the same point on the graph

substantially improved from the 25 % IHP cutoff threshold required by the uniform connector model.

In comparing the sensitivity and specificity of EAH predictions between the connector and VF models, the brain-skull displacement prediction metric generally improved the

sensitivity of the EAH predictions, but often decreased the specificity of the predictions (Table 11). Cortical principal stress, however, increased the overall sensitivity and specificity of EAH predictions by 14 and 15 %, respectively. Furthermore, predictions substantially improved in all regions except the posterior left which had a drop from 100 to 86 % in sensitivity and an increase from 93 to 100 % in specificity. From these data, it is clear that cortical principal stress was the best predictor of hemorrhage. The lack of difference between the low- and high-VF model for this metric suggests that this metric is robust enough to handle natural variations in arachnoid trabeculae volume fraction between animals.

4 Discussion

In this study, multiscale modeling was used to investigate the influence of PAC microstructure variability on overall brain mechanics, and on predictions of intracranial hemorrhage in a porcine model of TBI. Incorporating representative solid elements that utilize transversely isotropic properties based on the varying density of arachnoid trabeculae and vasculature within the brain resulted in an increase in localized variability, or “hot spots” of stress, along the brain compared to the previous connector model that exhibited a more uniform cortical stress pattern. This is an intriguing finding, as it illustrates that despite the small volumetric contribution

Table 11 Sensitivity and specificity (respectively, in percent) for all models

FE Metric	Connector model (25 % IHP threshold)	New VF models (1 % IHP threshold)			
	Top 1 % connector strain	Top 5 % brain–skull displacement		Top 5 % principal stress	
Low or High VF	n/a	Low VF	High VF	Low VF	High VF
FE Metric Value	0.31 mm/mm	0.373 mm	0.284 mm	46.6 kPa	44.7 kPa
Overall	80/85	94/69	94/73	94/100	94/100
Anterior Left	63/80	85/100	77/100	92/100	92/100
Anterior Right	80/88	92/83	100/67	100/100	100/100
Posterior Left	100/93	93/25	93/0	86/100	86/100
Posterior Right	0/76	92/100	100/100	92/100	92/100
Midline	90/100	100/100	100/83	100/100	100/100

of the PAC to the intracranial space, the microstructural variability has substantial impact on brain mechanics during head rotation. Furthermore, the data suggest that the variability may be influential on localized predictions of intracranial hemorrhage.

Two subject-specific models were created to evaluate the effect of subject to subject variation in VF and resulting brain mechanics. The regional volume fractions differed by as much as 15 % between the two models, but the volume fractions averaged across the entire brain of each subject only differed by 5 %. This is representative of our previous OCT imaging findings that found a 4.8 % maximum difference in arachnoid trabeculae volume fraction across five animals. The two animals used in this study were not part of the previous imaging study. The VF model with the higher volume fraction exhibited lower brain–skull displacement and cortical principal stress values compared to the lower VF model. This is likely due to the increased tethering between the brain and skull in the high-VF model. These differences resulted in subject-specific injury threshold values for each hemorrhage prediction metric. Brain–skull displacement was more affected by subject variability and resulted in slightly different sensitivities and specificities for some regions of the brain when predicting intracranial hemorrhage with the low- and high-VF model. As can be observed in Table 10, cortical principal stress had less variation between the subject-specific variability and resulted in the same sensitivities and specificities, regardless of the model used (Table 11). The different results between the two prediction metrics was surprising, given that both were pulled from the same brain surface nodes (the displacement data additionally pulled from the skull surface nodes). One possible explanation for this is that brain–skull relative displacement is a value calculated purely from the interactions between the two surfaces, while the stress metric was determined from the first layer of brain elements and will be influenced by the deeper structures of the brain. The stress metric may thus possess a smoother profile and lead to less false positives and false negatives, giving

it higher sensitivity and specificity values. We conclude that cortical principal stress is a more robust prediction metric. Of course, this conclusion might not hold true for animals with arachnoid trabeculae volume fractions outside of our observed range.

Regardless of the subject-specific differences, both VF models showed a more consistent ability to correlate with the severity of regional intracranial hemorrhage relative to the existing cortical connector model, especially for cortical principal stress. The brain–skull displacement metric dramatically increased both sensitivity and specificity for some regions, but dramatically decreased both parameters for other regions. This resulted in an overall increase in the sensitivity of the prediction from 80 % in the previous uniform connector model to 94 % in the VF model. However, the overall specificity of the brain–skull displacement metric decreased from 85 to 69 % and 73 % for the low- and high-VF model, respectively. In contrast, using cortical principal stress as a predictor for intracranial hemorrhage substantially increased overall sensitivity and specificity by 14 and 15 %, respectively. Regionally, predictions improved by as much as 92 %, and there was only a single region where there was a decrease in performance (100–86 % sensitivity in the posterior left region). This decrease was offset by an increase from 93 to 100 % specificity in the same region. Even more intriguing was that the required IHP cutoff threshold, which defined whether a region in the animal's brain was considered positive for hemorrhage, was markedly reduced from 25 to 1 %. We conclude that incorporating the natural variability of arachnoid trabeculae volume fraction increases the overall ability of the model to predict smaller regions or hemorrhage, or milder traumatic brain injuries.

The finding that cortical principal stress is a better predictor of regional intracranial hemorrhage is interesting considering that maximum values of cortical principal stress did not significantly differ between many of the regions. Upon further post hoc analysis of regional intracranial hemorrhage patterns, bleeding in the brain following sagittal rotation was

highest in the midline regions, and then uniformly distributed across anterior and posterior left/right lobes. Following axial head rotation, intracranial hemorrhage was also highest in the midline region, and then distributed across the anterior lobes. Levels of intracranial hemorrhage in the posterior lobes were more sporadic. Maximum brain–skull displacement was consistently higher in the midline and the posterior lobes, which is likely why it did not perform as well as a predictor of hemorrhage. A post hoc correlational analysis between maximum cortical principal stress and the percentage of IHP indicated that there was a significant correlation between increasing principal stress and increasing levels of hemorrhage ($p < 0.001$), but only moderately so (correlation coefficient = 0.676). Performing a similar post hoc correlation analysis of brain–skull displacement and IHP also showed a significant correlation ($p < 0.001$), but the correlation was lower (correlation coefficient = 0.484). What this suggests is that cortical principal stress is an accurate predictor of the presence/absence of regional intracranial hemorrhage, but may only weakly predict the severity of the hemorrhage. Inclusion of microstructural anatomy specific to the midline region of the model may improve these correlations.

The VF models provided substantial improvements over our previously published model, but there are several limitations in the development of the microscale PAC models used to generate the representative solid elements. Nonlinear strain and strain rate responses of brain tissue were well represented with hyperelastic and viscoelastic properties in the macroscale model, but the microscale PAC models were composed of linear elastic constitutive models. Based on the data from Jin et al. (2007b), a linear elastic model was likely appropriate for arachnoid trabeculae, but the pia and arachnoid membranes have been shown to exhibit nonlinear behavior (Aimedieu and Grebe 2004; Jin et al. 2006). Given that these membranes were thin and effectively fixed to the dura and brain when the RSEs were implemented into the macroscale model, we speculate that the assumption of linearity in these tissues likely had minimal effect on the findings. However, Jin et al. report that the PAC is rate-dependent in traction (2007b), suggesting the arachnoid trabeculae may also be rate dependent. Viscoelastic properties were not included in the PAC model. Instead, the highest strain rate (500 s^{-1}) evaluated by Jin et al. was used as the basis for the properties of the arachnoid trabeculae. Future work should consider incorporating intrinsic rate-dependent behavior.

One other limitation in the PAC models was the exclusion of cerebrospinal fluid (CSF). Physiologically, the compressive response of the PAC is dominated by the fluid buoyancy of the CSF. This suggests that the model developed in this study is not appropriate for head impact or blast-associated predictions. We simulated rapid, non-impact head rotations with the assumption that the influence of the CSF would

be minimal. In reality, there is likely some PAC compression during the head rotation, even without impact. Despite this limitation, our correlations with intracranial hemorrhage were still excellent. Therefore, we propose that subarachnoid and subdural hemorrhage are strongly correlated with vasculature tension during brain–skull displacement rather than compression of the brain against the skull. The influence of CSF in head impact or blast exposure are future investigations required to broaden the applicability of this model to multiple injury modalities.

Gyral folds were not included in the macroscale or microscale simulations, and the localized cortical stress distribution was a function of the PAC material property changes and not brain surface undulation. Inclusion of gyral folds in the macroscale model would likely alter the stress distributions reported in this study, but we hypothesize that these changes would be fairly localized and not affect our overall regional predictions of hemorrhage. Cloots et al. (2008) investigated the effect of gyral inclusion on cortical stress magnitude. They reported stress concentrations near the endpoints of the gyral folds (deep within the cortex) that increased the maximum equivalent stress by 31–84%. However, the average equivalent stress of the cortex was only 8–10% greater than a homogeneous model. The average stress on the surface of the brain was minimally increased, which suggests that the inclusion of gyral folds may increase our hemorrhage prediction thresholds slightly, but not our regional distribution of stress.

Even with these limitations, the results show that during head rotation, the variability of the structures will have significant influence on the pattern of cortical stress and the prediction of intracranial hemorrhage. One of the ultimate goals of TBI biomechanics research is to be able to relate head kinematic data (e.g., accelerations, velocities) to predictions of TBI. Improvements in technology have allowed researchers to begin collecting biomechanical data on the forces leading to concussion and mild TBI in athletic populations (Broglia et al. 2010; Crisco et al. 2010, 2011; Higgins et al. 2007). However, interpretation of this data has been challenging because of the large injury variability among players and the multiple confounding factors such as history of impact and timing between impacts. The findings from our study suggest that the natural variability in the brain–skull interface could also contribute to the variability of TBI. At present, there are no in vivo imaging methods to assess arachnoid trabeculae in humans. However, investigation of the PAC microstructures postmortem in a human population may also conclude that a single PAC architectural density is sufficient to predict localized intracranial hemorrhage across subjects. At present, it is unclear how much PAC variation exists in the human population and whether this variation is affected by age and/or gender.

5 Conclusion

A computationally efficient method of implementing microscale level details of the PAC into a macroscale whole-head model was developed. The macroscale simulations showed a marked improvement in predicting regional hemorrhage when using a variable VF PAC (as compared to a strictly homogenous model). These new models were able to predict hemorrhage at a much lower cutoff value, as well as with higher sensitivity and specificity overall, when using cortical principal stress as our injury metric. These data suggest that the PAC does have a significant effect on brain biomechanics. We conclude that including a biofidelic PAC substructure variability in FE models of the head is essential for improved predictions of hemorrhage at the brain/skull interface.

Acknowledgments The authors would like to thank the Primary Children's Medical Center Foundation Early Career Award for their financial support of this work.

Compliance with ethical standards

Funding This study was funded by the Primary Children's Medical Center Foundation.

Conflict of Interest All authors have no conflicts of interest to report

References

- Aimedieu P, Grebe R (2004) Tensile strength of cranial pia mater: preliminary results. *J Neurosurg* 100:111–114
- Armstrong DL, Bagnall C, Harding JE, Teele RL (2002) Measurement of the subarachnoid space by ultrasound in preterm infants. *Arch Dis Child Fetal Neonatal Ed* 86:F124–F126
- Barber T, Brockway J, Higgins L (1970) The density of tissues in and about the head. *Acta Neurol Scand* 46:85–92
- Broglio S, Schnebel B, Sosnoff J, Shin S, Feng X, He X, Zimmerman J (2010) The biomechanical properties of concussions in high school football. *Med Sci Sports Exerc* 42:2064–2071
- Bylski DI, Kriewall TJ, Akkas N, Melvin JW (1986) Mechanical behavior of fetal dura mater under large deformation biaxial tension. *J Biomech* 19:19–26
- Cloots R, van Dommelen J, Geers M (2012) A tissue-level anisotropic criterion for brain injury based on microstructural axonal deformation. *J Mech Behav Biomed Mater* 5:41–52
- Cloots R, van Dommelen J, Kleiven S (2013) Multi-scale mechanics of traumatic brain injury: predicting axonal strains from head loads. *Biomech Model Mechanobiol* 12:137–150
- Cloots R, van Dommelen J, Nyberg T, Kleiven S, Geers M (2011) Micro-mechanics of diffuse axonal injury: influence of axonal orientation and anisotropy. *Biomech Model Mechanobiol* 10:413–422
- Cloots RJH, Gervaise HMT, van Dommelen JAW, Geers MGD (2008) Biomechanics of traumatic brain injury: influences of the morphologic heterogeneities of the cerebral cortex. *Ann Biomed Eng* 36:1203–1215
- Coats B, Eucker S, Sullivan S, Margulies S (2012) Finite element model predictions of intracranial hemorrhage from non-impact, rapid head rotations in the piglet. *Int J Dev Neurosci* 30:191–200
- Coats B, Margulies S (2006a) High rate material properties of infant cranial bone and suture. *J Neurotrauma* 23(8):1222–1232
- Coats B, Margulies S (2006b) Material properties of porcine parietal cortex. *J Biomech* 39:2521–2525
- Couper Z, Albermani F (2008) Infant brain subjected to oscillatory loading: material differentiation, properties, and interface conditions. *Biomech Model Mechanobiol* 7(2):105–125
- Crisco J, Fiore R, Beckwith J, Chu J, Per Gunnar B, Duma S, McAllister T, Duhaime A, Greenwald R (2010) Frequency and location of head impact exposures in individual collegiate football players. *J Athl Train* 45:549–559
- Crisco J, Wilcox B, Beckwith J, Chu J, Duhaime A, Rowson S, Duma S, Maerlender A, McAllister T, Greenwald R (2011) Head impact exposure in collegiate football players. *J Biomech* 44:2673–2678
- Eucker S, Smith C, Ralston J, Friess S, Margulies S (2011) Physiological and histopathological responses following closed rotational head injury depend on direction of head motion. *Exp Neurol* 227:79–88
- Faul M, Xu L, Wald M, Coronado V (2010) Traumatic brain injury in the united states: emergency department visits, hospitalizations, and deaths. 2002–2006
- Frankel DA, Fessel DP, Wolfson WP (1998) High resolution sonographic determination of the normal dimensions of the intracranial extraaxial compartment in the newborn infant. *J Ultrasound Med* 17:411–415
- Galford J, McElhaney J (1970) A viscoelastic study of scalp, brain, and dura. *J Biomech* 3:211–221
- Giordano C, Cloots R, van Dommelen J, Kleiven S (2014) The influence of anisotropy on brain injury prediction. *J Biomech* 47:1052–1059
- Hagmann CF, Robertson NJ, Acolet D, Nyombi N, Ondo S, Nakakeeto M, Cowan FM (2011) Cerebral measurements made using cranial ultrasound in term ugandan newborns. *Early Hum Dev* 87:341–347
- Higgins M, Halstead P, Snyder-Mackler L, Barlow D (2007) Measurement of impact acceleration: mouthpiece accelerometer versus helmet accelerometer. *J Athl Train* 42:5–10
- Ji S, Ghadyani R, Bolander R, Beckwith J, Ford J, McAllister T, Flashman L, Paulsen K, Ernstrom K, Jain S, Raman R, Zhang L, Greenwald R (2014) Parametric comparisons of intracranial mechanical responses from three validated finite element models of the human head. *Ann Biomed Eng* 42:11–24
- Jin X, Lee JB, Leung LY, Zhang L, Yang KH, King AI (2006) Biomechanical response of the bovine pia-arachnoid complex to tensile loading at varying strain-rates. *Stapp Car Crash J* 50:637–649
- Jin X, Ma C, Zhang L, Yang K, King A, Dong G, Zhang J (2007) Biomechanical response of the bovine pia-arachnoid complex to normal traction loading at varying strain rates. *Stapp Car Crash J* 51:115–125
- Jin X, Ma C, Zhang L, Yang KH, King AI (2007) Biomechanical response of the bovine pia-arachnoid complex to normal traction loading at varying strain rates. *Stapp Car Crash J* 51:115–126
- Jin X, Yang KH, King AI (2011) Mechanical properties of bovine pia-arachnoid complex in shear. *J Biomech* 44:467–474
- Kuijpers A, Claessens M, Sauren A (1995) The influence of different boundary conditions on the response of the head to impact: a two-dimensional finite element study. *J Neurotrauma* 12:715–724
- Lam WWM, Ai VH, Wong V, Leong LLY (2001) Ultrasonographic measurement of subarachnoid space in normal infants and children. *Pediatr Neurol* 25:380–385
- Ma C, Jin X, Zhang J, Huang S (2008) Development of the pia-arachnoid complex finite element model. *Bioinformatics and Biomedical Engineering, ICBBE, the 2nd International Conference*. Shanghai, China
- McAllister T, Ford J, Ji S, Beckwith J, Flashman L, Paulsen K, Greenwald R (2011) Maximum principal strain and strain rate associated with concussion diagnosis correlates with changes in corpus callosum white matter indices. *Ann Biomed Eng* 10:127–140

- Monson KL, Goldsmith W, Barbaro NM, Manley GT (2005) Significance of source and size in the mechanical response of human cerebral blood vessels. *J Biomech* 35:737–744
- Nahum A, Smith R (1977) Intracranial pressure dynamics during head impact. Proceedings of the 21st stapp car crash conference. SAE Paper No. 770922
- Pang Q, Lu X, Gregersen H, von Oettingen G, Astrup J (2001) Biomechanical properties of porcine cerebral bridging veins with reference to the zero-stress state. *J Vasc Res* 38:83–90
- Paolini B, Danelson K, Geer C, Stitzel J (2009) Pediatric head injury prediction: investigating the distance between the skull and the brain using medical imaging. *Biomed Sci Inst* 45:161–166
- Persson C, Evans S, Marsh R, Summers JL, Hall RM (2010) Poisson's ratio and strain rate dependency of the constitutive behavior of spinal dura mater. *Ann Biomed Eng* 38:975–983
- Prange M, Margulies S (2002) Regional, directional, and age-dependent properties of brain undergoing large deformation. *J Biomech Eng* 124:244–252
- Roth S, Raul JS, Willinger R (2008) Biofidelic child head fe model to simulate real world trauma. *Comput Methods Prog Biomed* 90:262–274
- Sabet A, Christoforou E, Zatlín B, Genin G, Bayly P (2008) Deformation of the human brain induced by mild angular head acceleration. *J Biomech* 41(2):307–315
- Scott G (2014) Anatomy and biomechanics of the pia-arachnoid complex. Mechanical Engineering, University of Utah, Salt Lake City
- Scott G, Coats B (2015) Microstructural characterization of the pia-arachnoid complex using optical coherence tomography. *IEEE Trans Med Imag*
- Sullivan S, Eucker SA, Gabrieli D, Bradfield C, Coats B, Maltese M, Lee JY, Smith C, Margulies S (2015) White matter tract oriented deformation predicts traumatic axonal brain injury and reveals rotational direction-specific vulnerabilities. *Biomech Model Mechanobiol* 14(4):877–896
- Takhounts E, Ridella S, Hasija V, Tannous R, Campbell J, Malone D, Danelson K, Stitzel J, Rowson S, Duma S (2008) Investigation of traumatic brain injuries using the next generation of simulated injury monitor (simon) finite element head model. *Stapp Car Crash J* 52:1–31
- Wittek A, Omori K (2003) Parametric study of effects of brain-skull boundary conditions and brain material properties on responses of simplified finite element brain model under angular acceleration impulse in sagittal plane. *JSME Int J Ser C Mech Syst Mach Elem Manuf* 46:1388–1399
- Wright R, Post A, Hoshizaki B, Ramesh K (2013) A multiscale computational approach to estimating axonal damage under inertial loading of the head. *J Neurotrauma* 30:102–118
- Wright R, Ramesh K (2012) An axonal strain injury criterion for traumatic brain injury. *Biomech Model Mechanobiol* 11:245–260
- Zhang L, Bae J, Hardy W, Monson K, Manley G, Goldsmith W, Yang K, King A (2002) Computational study of the contribution of the vasculature on the dynamic response of the brain. *Stapp Car Crash J* 46:145–163
- Zhang L, Yang K, Dwarampudi R, Omori K, Li T, Chang K, Hardy W, Khalil T, King A (2001) Recent advances in brain injury research: a new human head model development and validation. *Stapp Car Crash J* 45:369–394
- Zoghi-Moghadam M, Sadegh A (2009) Global/local head models to analyze cerebral blood vessel rupture leading to asdh and sah. *Comput Methods Biomech Biomed Eng* 12:1–12